

---

# In-plane dynamic buckling of duoskelion beam-like structures: discrete modeling and numerical results

**Emilio Turco** 

*Department of Architecture, Design and Urban planning (DADU), University of Sassari, Alghero, Italy; International Research Center on Mathematics and Mechanics of Complex Systems (M&MOCS), University of L'Aquila, L'Aquila, Italy*

**Emilio Barchiesi**

*Universidad de Lima, Instituto de Investigación Científica, Santiago de Surco, Peru; École Nationale d'Ingénieurs de Brest, Brest, France; Department of Architecture, Design and Urban planning (DADU), University of Sassari, Alghero, Italy*

**Francesco dell'Isola**

*Department of Civil, Construction-Architectural and Environmental Engineering (DICEAA) and International Research Center on Mathematics and Mechanics of Complex Systems (M&MOCS), University of L'Aquila, L'Aquila, Italy*

## Abstract

In this contribution, a previously introduced discrete model for studying the statics of duoskelion beam-like structures is extended to dynamics. The results of numerical simulations performed using such an extended model are reported to discuss the in-plane dynamic buckling of duoskelion structures under different loading and kinematic boundary conditions. The core instrument of the analysis is a discrete beam element, which, in addition to flexure, also accounts for extension and shearing deformations. Working in the setting of dynamics, inertial contributions are taken into account as well. A stepwise time integration scheme is employed to reconstruct the complete trajectory of the system, namely before and after buckling. It is concluded that the duoskelion structure exhibits exotic features compared with classical beam-like structures modeled at macro-scale by Euler–Bernoulli's model.

## Keywords

Mechanics of metamaterials, discrete models, dynamic nonlinear analysis, stepwise analysis, duoskelion structures

---

## Corresponding author:

Emilio Turco, Department of Architecture, Design and Urban planning (DADU), University of Sassari and International Research Center on Mathematics and Mechanics of Complex Systems (M&MOCS), University of L'Aquila, Italy.  
Email: emilio.turco@uniss.it

## I. Introduction

Recent research in the field of metamaterials [1–3] has stimulated the rediscovery and improvement of previously developed models of structural elements—such as beams [4–12], plates [13–16], shells [17–21], and solids [22–24]—which have been adapted to study the exotic mechanical behaviors exhibited by metamaterials.

In the field of metamaterials, a good understanding of the influence of microscopic constituents on overall behavior has indeed proven to be crucial. Such an understanding can be obtained by means of coarse-grained continuum models informed from the micro-structure, such as second [25–28] or higher [29–31] displacement gradient models, micromorphic models [32–35], and non-local integral models [36–39].

These coarse-grained models can be obtained using many techniques: through direct phenomenological formulations [40–45], asymptotic [46–48] or non-asymptotic [49] homogenization techniques, etc. These models allow consideration of simple macro-scale geometries, as the complex micro-scale is smeared out. While being computationally advantageous, continuum macro-scale models have many limitations, which are linked to the identification of parameters [50–54] and the often-insufficient scale separation [55], which makes the macro-scale continuity assumption unsuitable, as it constrains the kinematics too much.

To validate and fit continuum models [56, 57], as well as to improve the accuracy of the modeling, one should resort to more refined modeling strategies, which better take the micro-structure into account. In beam lattices [58–62], the use of models to represent each element of the lattice is required for this purpose. In this regard, two non-full-scale approaches are possible in principle: the first considers interactions between nodes of the lattice as well-described by springs, i.e. by an intrinsically discrete theory, be they extensional or rotational [63, 64]; the second utilizes a continuum beam model derived from the homogenization of the aforementioned spring model to describe each interaction [65–67]. Nevertheless, the continuum approach might need to be suitably discretized to reconstruct the solution numerically, especially if problems with a certain degree of complexity must be studied.

Procedurally, when variationally formulated, and if only elastic phenomena are taken into account, both meso-scale approaches rely on the definition of the strain energy for static problems, while the kinetic energy must also be defined for dynamic ones.

An example of these concepts is provided by so-called pantographic fabrics, which are metamaterials whose study has encompassed mathematical [68] and theoretical [69] mechanics issues, as well as experimental and manufacturing aspects. Another example is given by the structure that is going to be studied in the following. Indeed, this study concerns an articulated beam structure constituted of elements arranged according to a specific chirality [70], first introduced in [71]. The structure as a whole, owing to its slenderness and geometry, is also referred to as a duoskelion beam. The name duoskelion is a neologism, which is inspired by Greek and means *two-legged*. When micro-scale stiffnesses are suitably chosen so as to have a strong mechanical contrast at the micro-scale, duoskelion beams can be employed as mechanical switches with customizable on–off traction loading thresholds. Additionally, in compression, they are capable of strongly coupling transverse and axial motions, and they could be designed to show a monodirectional response, i.e. to be extensible but incompressible, see again [71].

In the same spirit of [72]—which deals with an intrinsically discrete formulation equivalent to Euler–Bernoulli’s beam model in a three-dimensional setting—and following [73]—which extends such a formulation to extensible and shear-deformable beams—in this study we consider an intrinsically discrete meso-scale beam model, taking into account shear deformations and, more particularly, a model that, in the linear regime, is equivalent to the so-called Timoshenko–Ehrenfest model, see [74]. Inertial contributions are taken into account as well. A stepwise time integration scheme is employed to reconstruct the complete trajectory of the system, namely before and after buckling.

The paper is organized as follows. In Section 2, the discrete beam element, on which we base the entire analysis, is introduced in the general three-dimensional setting. At first, we define the kinematics. Then, we introduce the strain and kinetic energies. In Section 3, we report on the performed numerical simulations. At first, we provide reasonably realistic values of the model parameters by making use of the Saint-Venant formulas. Then we show (Section 3) results illustrating the dynamic buckling of beam-like duoskelion structures for different end conditions. Subsequently, the influence of the loading velocity on the results is briefly discussed, as well as the results of a pull test. Finally, an analysis of sensitivity with respect to stiffness parameters is conducted. In Section 4, we present our conclusions and provide some outlook for further work.

## 2. Discrete shearable beam formulation in three dimensions

The mechanical response of a system is completely defined by its strain energy in the static case. For dynamic problems, in addition, one should also define the system's kinetic energy.

Indeed, the specification of these two energies completely defines the Lagrangian of the system, and hence the system's trajectories. While this is evidently true from the theoretical point of view, finding the aforementioned trajectories in the nonlinear regime can be a formidable—if not sometimes impossible—task, in both statics and dynamics, requiring the development and utilization of suitable tools. For an in-depth discussion of these topics, see [75–77]. In addition, see also [72], which treats a discrete model of an inextensible and unshearable beam in the three-dimensional setting, and [73], which deals with a discrete model of an extensible and shearable beam in the two-dimensional setting.

Next, we define, first, the strain energy and, successively, the kinetic energy of the considered discrete beam element used to model the duoskelion structure.

### 2.1. Strain energy

In the three-dimensional setting, a discrete one-dimensional beam model consists of a polygonal line moving in space. A node of such a polygonal line is endowed with a cross-section  $A$ , which can move in three dimensions, whose barycenter is the position occupied by the node itself. Such a position  $\mathbf{r}_C$  fulfills the following equation:

$$\int_A (\mathbf{r} - \mathbf{r}_C) dA = \mathbf{0}, \quad (1)$$

where the quantity  $\mathbf{r}$  is the position of a generic point lying on the cross-section  $A$ , with which a generic node of the polygonal line—the discrete beam—is endowed.

Clearly, each line segment could be replaced by more line segments, introducing further nodes and giving a so-called  $h$ -refinement or *enhanced* description [78]. The cross-sections which the nodes are endowed with are all assumed to be rigid, i.e. they can only rotate and translate.

From now on, nodes will be indicated using the symbol  $P_n$  or  $p_n$  (Figure 1). Capital and lowercase letters are referred to the reference and current configurations, respectively, while the subscript  $n$  labels the considered node. Each line segment, in brief a link, connecting two consecutive nodes is equipped—in the reference configuration—with three mutually orthogonal unit vectors  $\mathbf{D}_{1,n}$ ,  $\mathbf{D}_{2,n}$ , and  $\mathbf{D}_{3,n}$ . The first of these vectors is parallel to the link that connects two end nodes. In formulas, we have

$$\mathbf{D}_{1,n} = \frac{P_{n+1} - P_n}{\|P_{n+1} - P_n\|}. \quad (2)$$

The unit vectors  $\mathbf{D}_{2,n}$  and  $\mathbf{D}_{3,n}$  are two orthogonal vectors in the plane orthogonal to  $\mathbf{D}_{1,n}$ . Generally, it is convenient to choose  $\mathbf{D}_{2,n}$  and  $\mathbf{D}_{3,n}$  along the direction of the principal axes of the beam's cross-section.

We assume that the proper orthogonal tensor  $\mathbf{Q}_n$  transforms  $\mathbf{D}_{i,n}$  in  $\mathbf{d}_{i,n}$  ( $i = 1, 2, 3$ ), that is,

$$\mathbf{d}_{i,n} = \mathbf{Q}_n \mathbf{D}_{i,n}. \quad (3)$$

The strain measures for extension and shear deformations are defined starting from the following vectorial quantity:

$$\Delta \mathbf{w}_{n+1} = (p_{n+1} - p_n) - \|P_{n+1} - P_n\| \mathbf{Q}_n \mathbf{D}_{1,n}, \quad (4)$$

that is, the difference vector between  $(p_{n+1} - p_n)$  and  $\|P_{n+1} - P_n\| \mathbf{Q}_n \mathbf{D}_{1,n}$ . Note that the second term of this definition comes from the rigid-body motion, indeed the rotation  $\mathbf{Q}_n$ , of the link between nodes  $n$  and  $n + 1$  (the  $n$ th link). Furthermore, the following proper orthogonal tensor:

$$\mathbf{L}_{n+1} = \mathbf{Q}_{n+1} \mathbf{Q}_n^T - \mathbf{I}. \quad (5)$$

is defined as a strain measure for the bending and torsion of the beam. Note that, if  $\mathbf{Q}_n$  is equal to  $\mathbf{Q}_{n+1}$ , there is no relative rotation between the  $n$ th and  $(n + 1)$ th links, and  $\mathbf{L}_{n+1}$  is the null tensor. The orthogonal tensor  $\mathbf{Q}_{n+1} \mathbf{Q}_n^T$  will henceforth be called the tensor of the relative rotation between the  $n$ th and  $(n + 1)$ th links.

From the vectorial quantity introduced in equation (4), we can define a strain measure accounting for the extension of the beam and two strain measures accounting for its shearing deformations. These add up to the

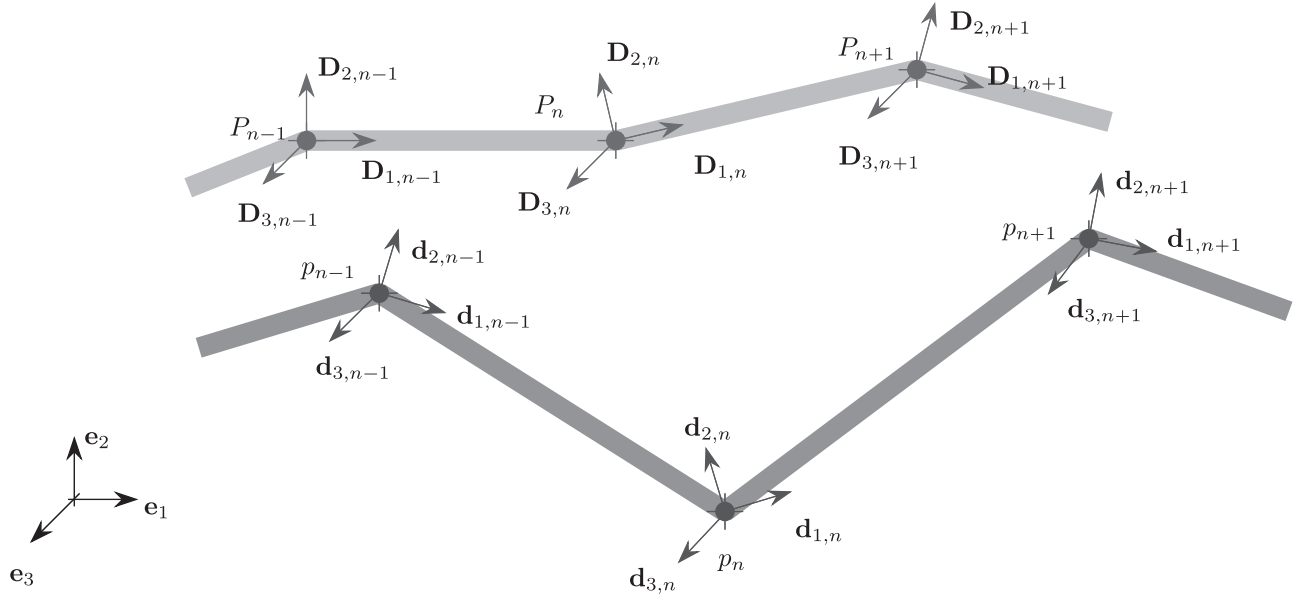


**Figure 1.** Kinematics of the beam model: reference (light gray) and current (dark gray) configurations.

previously defined strain measures accounting for bending and torsional deformations of the beam. The strain measure accounting for extension is defined as

$$\Delta \mathbf{w}_{n+1}^{\text{ext}} = (p_{n+1} - p_n) \left( 1 - \frac{\|P_{n+1} - P_n\|}{\|p_{n+1} - p_n\|} \right), \quad (6)$$

and, accordingly, the shearing strain is defined as being given by the following vectorial quantity:

$$\Delta \mathbf{w}_{n+1}^{\text{shr}} = \Delta \mathbf{w}_{n+1} - \Delta \mathbf{w}_{n+1}^{\text{ext}}. \quad (7)$$

Customarily, when such a vectorial quantity—a similar one, in fact—is manipulated by expressing it through its components, such components are obtained by projection on the principal directions of the beam's cross-section.

To deal more easily with bending and torsion deformations, it is convenient to recall Rodrigues' formula. Such a formula provides a closed-form expression of any arbitrary rotation tensor  $\mathbf{Q}$  in terms of a unit vector  $\mathbf{e}$ , which defines the axis of rotation, and of the rotation angle  $\varphi$ :

$$\mathbf{Q} = \cos \varphi \mathbf{I} + (1 - \cos \varphi) \mathbf{e} \otimes \mathbf{e} + \sin \varphi \mathbf{E}, \quad (8)$$

where the tensor  $\mathbf{E}$  is defined by the relation  $\mathbf{E}\mathbf{u} = \mathbf{e} \times \mathbf{u}$  for any vector  $\mathbf{u}$ . Starting from Rodrigues' formula (equation (8)), simple calculations give the following two relationships:

$$\begin{aligned} 2 \cos \varphi &= \text{tr}(\mathbf{Q}) - 1, \\ 2 \sin \varphi \mathbf{e} &= \mathbf{Q}_\times, \end{aligned} \quad (9)$$

where  $\text{tr}(\cdot)$  is the trace operator and  $\mathbf{Q}_\times$  is the vectorial invariant of  $\mathbf{Q}$ .<sup>1</sup>

Using Rodrigues' formula, we can thus compute the rotation vector  $\boldsymbol{\varphi}$  associated with the rotation tensor  $\mathbf{Q}$ , namely:

$$\boldsymbol{\varphi} = \varphi \mathbf{e}, \quad (10)$$

which is a convenient quantity to deal with in place of the rotation tensor itself. By using equation (9), we can find the rotation vector  $\Delta \boldsymbol{\varphi}_{n+1}$  associated with the relative rotation tensor  $\mathbf{Q}_n^T \mathbf{Q}_{n+1}$  in the strain measure (equation (5)).

The strain energy associated with the aforementioned strain measures can be written as

$$2\mathcal{S}_{n+1} = \begin{bmatrix} \Delta \mathbf{w}_{n+1} \\ \Delta \boldsymbol{\varphi}_{n+1} \end{bmatrix} \cdot \mathbf{A}_{n+1} \begin{bmatrix} \Delta \mathbf{w}_{n+1} \\ \Delta \boldsymbol{\varphi}_{n+1} \end{bmatrix}, \quad (11)$$

where the stiffness matrix  $\mathbf{A}_{n+1}$  collects the stiffness parameters of the beam segment between nodes  $n$  and  $n + 1$ . In general, the matrix  $\mathbf{A}_{n+1}$  might be nondiagonal, thus allowing all the desired mechanical couplings.

## 2.2. Kinetic energy

To complete the description of the discrete model introduced in the previous section, we need to define the kinetic energy of an elementary part of the beam. When such a definition is given, the computation of the kinetic energy of the whole beam will be simply accomplished by summing up all the elementary contributions.

Again, to simplify the formulas, only the link in between nodes  $n$  and  $n + 1$  is to be considered. Additionally, a continuous and uniform distribution of cross-sections is considered along each link. In the reference configuration, these cross-sections are assumed to be orthogonal to the link, whose points are their centroids. A generic centroid will be denoted with the symbol  $C$ . Additionally, the cross-sections, which are continuously distributed along a given link, are all assumed to be rigid, i.e. they can only rotate and displace.

The current position of a point  $C$  belonging to the link between nodes  $n$  and  $n + 1$  can be written as

$$\mathbf{r}(t) = \mathbf{R}_C + \mathbf{u}_C(t) + \mathbf{Q}(t)\mathbf{Z}, \quad (12)$$

where  $\mathbf{R}_C$  is the position—in the reference configuration—of the cross-section centroid  $C$ ,  $\mathbf{u}_C$  is the displacement of  $C$ ,  $\mathbf{Q}$  is the tensor describing the rotation of the cross-section, and  $\mathbf{Z}$  is the position of an arbitrary point  $Z$  belonging to the cross-section in the reference configuration. From equation (12), we can compute the Lagrangian velocity (dots indicate the time derivative):

$$\dot{\mathbf{r}}(t) = \dot{\mathbf{u}}_C(t) + \dot{\mathbf{Q}}(t)\mathbf{Z}. \quad (13)$$

By using the proper orthogonality property of the rotation tensor  $\mathbf{Q}$  defined previously, we can write the following identity:

$$\dot{\mathbf{Q}} = \dot{\mathbf{Q}}\mathbf{Q}^T\mathbf{Q}. \quad (14)$$

It is straightforward to show that the tensor  $\dot{\mathbf{Q}}\mathbf{Q}^T$  is a skew symmetric tensor.<sup>2</sup> Therefore, we can associate to  $\dot{\mathbf{Q}}\mathbf{Q}^T$  an axial vector, also known as the angular velocity vector:

$$\boldsymbol{\omega} = -\frac{1}{2}(\dot{\mathbf{Q}}\mathbf{Q}^T)_{\times}. \quad (15)$$

Hence, we can rewrite equation (13) in the following form:

$$\dot{\mathbf{r}}(t) = \dot{\mathbf{u}}_C(t) + \boldsymbol{\omega}(t) \times \mathbf{Q}(t)\mathbf{Z}, \quad (16)$$

where it is possible to recognize the translational,  $\dot{\mathbf{u}}_C(t)$ , and the rotational,  $\boldsymbol{\omega}(t) \times \mathbf{Q}(t)\mathbf{Z}$ , velocity contributions.

By means of this representation, we can compute the kinetic energy per unit link length:

$$2 \, d\mathcal{T} = \int_A \rho \dot{\mathbf{u}}_z \cdot \dot{\mathbf{u}}_z \, dA, \quad (17)$$

which, by using equation (16) and remembering that the centroid of a cross-section is characterized by the condition:

$$\int_A \mathbf{z} \, dA = \mathbf{0}, \quad (18)$$

can be rewritten as follows:

$$2d\mathcal{T} = \int_A \rho (\|\dot{\mathbf{u}}_c\|^2 + \|\boldsymbol{\omega} \times \mathbf{z}\|^2) \, dA. \quad (19)$$

By taking into account the elementary equality chain

$$\|\boldsymbol{\omega} \times \mathbf{z}\|^2 = (\|\boldsymbol{\omega}\| \|\mathbf{z}\| \sin(\widehat{\boldsymbol{\omega}, \mathbf{z}}))^2 = \|\boldsymbol{\omega}\|^2 \|\mathbf{z}\|^2 \left(1 - \left(\frac{\boldsymbol{\omega} \cdot \mathbf{z}}{\|\boldsymbol{\omega}\| \|\mathbf{z}\|}\right)^2\right) = (\boldsymbol{\omega} \cdot \boldsymbol{\omega})(\mathbf{z} \cdot \mathbf{z}) - (\boldsymbol{\omega} \cdot \mathbf{z})^2, \quad (20)$$

and making use of the definitions

$$m = \int_A \rho dA, \quad \mathbf{J}_c = \int_A \rho ((\mathbf{z} \cdot \mathbf{z})\mathbf{I} - \mathbf{z} \otimes \mathbf{z}) dA, \quad (21)$$

the kinetic energy per unit link length can be rewritten in a shorter form as:

$$2 \mathcal{T} = m \dot{\mathbf{u}}_c \cdot \dot{\mathbf{u}}_c + \boldsymbol{\omega} \cdot \mathbf{J}_c \boldsymbol{\omega}. \quad (22)$$

The inertia tensor  $\mathbf{J}_c$  appearing in this equation is defined in the current basis as

$$\mathbf{J}_c = \ell \begin{bmatrix} \int_A \rho(z_2^2 + z_3^2) dA & 0 & 0 \\ 0 & \int_A \rho z_3^2 dA & -\int_A \rho z_2 z_3 dA \\ 0 & -\int_A \rho z_2 z_3 dA & \int_A \rho z_2^2 dA \end{bmatrix}, \quad (23)$$

where  $\mathbf{z} = z_2 \mathbf{d}_2 + z_3 \mathbf{d}_3$ . We remark that, if the unit vectors  $\mathbf{d}_2$  and  $\mathbf{d}_3$  are chosen as to lie in the direction of the principal axes of inertia, then the inertia tensor  $\mathbf{J}_c$  is diagonal.

From equation (22), we can, at this point, easily derive the kinetic energy of the whole link:

$$\mathcal{T}_e = \frac{1}{2} \int_0^\ell (m \dot{\mathbf{u}}_C \cdot \dot{\mathbf{u}}_C + \boldsymbol{\omega} \cdot \mathbf{J}_C \boldsymbol{\omega}) ds. \quad (24)$$

Assuming a linear interpolation of the centroids' velocities between nodes  $n$  and  $n+1$ , we can write

$$\mathbf{u}_C(s) = \mathbf{B}_e \mathbf{u}_e, \quad (25)$$

utilizing the following definitions:

$$\mathbf{u}_e = \begin{bmatrix} \dot{\mathbf{u}}_n \\ \dot{\mathbf{u}}_{n+1} \end{bmatrix}, \quad \mathbf{B}_e = \begin{bmatrix} 1 - \frac{s}{\ell} & 0 & 0 & \frac{s}{\ell} & 0 & 0 \\ 0 & 1 - \frac{s}{\ell} & 0 & 0 & \frac{s}{\ell} & 0 \\ 0 & 0 & 1 - \frac{s}{\ell} & 0 & 0 & \frac{s}{\ell} \end{bmatrix} \quad (26)$$

Conversely, the angular velocity vector  $\boldsymbol{\omega}$  is assumed as uniform along each link. Therefore, the kinetic energy of a link between nodes  $n$  and  $n+1$  reads as:

$$\mathcal{T}_e = \frac{1}{2} (\dot{\mathbf{u}}_e \cdot \mathbf{M}_e^t \dot{\mathbf{u}}_e + \boldsymbol{\omega} \cdot \mathbf{M}_e^r \boldsymbol{\omega}), \quad (27)$$

where  $\mathbf{M}_e^t$  is the mass matrix related to the translation Lagrangian parameters and  $\mathbf{M}_e^r$  is the mass matrix related to the rotational Lagrangian parameters. The following expressions are assumed for the aforementioned mass matrices:

$$\mathbf{M}_e^t = \int_0^\ell m \mathbf{B}_e^T \mathbf{B}_e ds = \frac{m\ell}{6} \begin{bmatrix} 2 & 0 & 0 & 1 & 0 & 0 \\ 0 & 2 & 0 & 0 & 1 & 0 \\ 0 & 0 & 2 & 0 & 0 & 1 \\ 1 & 0 & 0 & 2 & 0 & 0 \\ 0 & 1 & 0 & 0 & 2 & 0 \\ 0 & 0 & 1 & 0 & 0 & 2 \end{bmatrix} \quad (28)$$

and

$$\mathbf{M}_e^r = \int_0^\ell \mathbf{J}_C ds = \ell \mathbf{J}_C. \quad (29)$$

---

### 3. Numerical simulations

In this section, we report on the results of numerical simulations performed with the model described in the previous section, as applied to the analysis of a specific duoskelion structure. With the considered duoskelion structure mainly extended in only one dimension, the performed tests were largely inspired from classical results available for the Euler–Bernoulli beam.

More specifically, after a preliminary discussion on the mechanical parameters—the stiffnesses and the inertial parameters—and their identification, we present results as obtained by varying

- (a) the conditions at the ends of the considered beam-like duoskelion structure,
- (b) the external loading rate,
- (c) the stiffnesses,

to study the sensitivity of the mechanical behavior with respect to these factors.

#### 3.1. Identification of the mechanical parameters

It is well known from the Saint-Venant results for an isotropic and homogeneous elastic prism in the linear regime that the elongation  $\Delta L$  is

$$\Delta L = \frac{NL}{EA},$$

where  $N$ ,  $L$ ,  $E$ , and  $A$  are the normal force on the bases, the length of the prism, the Young modulus, and the cross-sectional area, respectively. If we think of the prism as divided into  $n$  cells, each having length  $\ell = L/n$  and an equivalent extensional stiffness  $a$ , to identify such a parameter  $a$ , we can equate the elongation of the prism  $\Delta L$  with that of the  $n$  cells in series,

$$\Delta L = \frac{NL}{EA} = n \frac{N}{a},$$

from which the following simple relationship is found:

$$a = \frac{EA}{\ell}.$$

Considering that this estimate is based on assumptions—above all that of a linear regime—that could be far from being fulfilled in the considered problem, such an estimate of the stiffness  $a$  is surely a good starting point. With an analogous reasoning, we can estimate the bending stiffness  $b$  as

$$b = \frac{EJ}{\ell},$$

where  $J$  is the rotational inertia of the cross-section, and the shear stiffness  $c$ ,

$$c = \frac{GA^*}{\ell},$$

where  $G$  is the tangential elasticity modulus and  $A^*$  is the reduced cross-section area.

We consider a beam-like duoskelion structure made up of 20 unit cells, see Figure 2, in which, for illustrative purposes, only 10 cells are depicted. The parameters  $E$  and  $\rho$ , needed to identify the model parameters according to the previous discussion, are taken to be equal to those characterizing standard steel;  $E = 2.1 \times 10^6 \text{ N/mm}^2$  and  $\rho = 7850 \text{ kg/m}^3$ .

The considered duoskelion structure has a length  $L = 1 \text{ m}$  and a uniform square cross-section of side length 1 mm. Regarding the discrete mechanical modeling, vertical tracts of the duoskelion structure are discretized by means of three nodes, while horizontal tracts are discretized by means of two nodes. Therefore, the distance between two consecutive nodes is equal to  $\ell$  along the whole structure. From these data, also reported in Table 1, which makes use of the MKS system of units, not only can we estimate the stiffness parameters  $a$ ,  $b$ , and  $c$ , but we can also compute the cross-section area and inertia (see again Table 1).

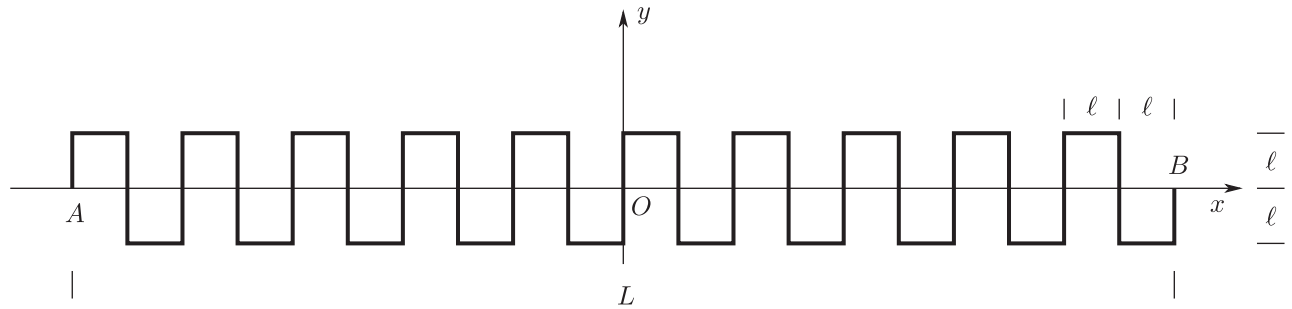


**Figure 2.** Geometry of a duoskelion beam-like structure with 10 unit cells.

**Table I.** Reference dataset. All quantities are expressed in the MKS system of units.

$L$	$n$	$a$	$b$	$c$	$\rho$	$A$	$J$
1	20	$84 \times 10^5$	0.7	$42 \times 10^5$	7850	$10^{-6}$	$8.3333 \times 10^{-14}$

### 3.2. Dynamic buckling for different end conditions

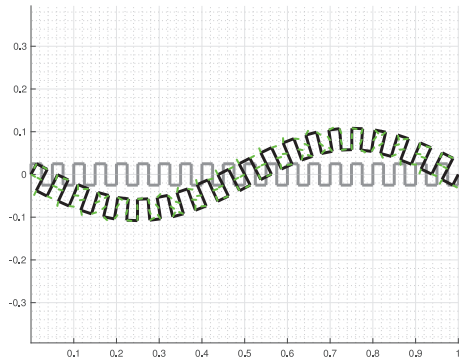
The first test is inspired by the simply supported Euler–Bernoulli’s beam column compression problem. A duoskelion structure with 20 unit cells is considered, where the left end ( $A$  in Figure 2) is hinged and the right end ( $B$  in Figure 2) is simply supported in the vertical direction, i.e. constrained by a roller to move only horizontally. Using the dataset reported in Table 1, we apply a compression load, varying in time with a linear law and having slope  $\dot{p}$ .

Before conducting numerical simulations for this case study, the first and last natural periods of the considered duoskelion structure for the applied kinematic conditions and considered model parameters must be computed to calibrate the numerical stepwise time integration scheme used herein, namely Casciaro’s scheme [63], appropriately. Figure 3 shows the first eight natural modes, along with the corresponding natural periods computed in the reference configuration. Natural modes are useful to understand the vibrations of the duoskelion structure, at least close to the reference configuration. From this modal analysis, we see that the first and last natural periods are  $T_1 = 0.9063$  s and  $T_n = 4.952 \times 10^{-7}$  s, respectively. Of the first eight modes, only the second and the eighth modes are extensional modes, all the others being bending modes. In Figure 3, as well as in all the following figures, the reference configuration of the duoskelion structure is represented in gray, while black and green colors are employed to represent the deformed configuration. More specifically, black is used to connect nodes’ current positions, while green arrows allow the cross-section rotation to be visualized graphically.

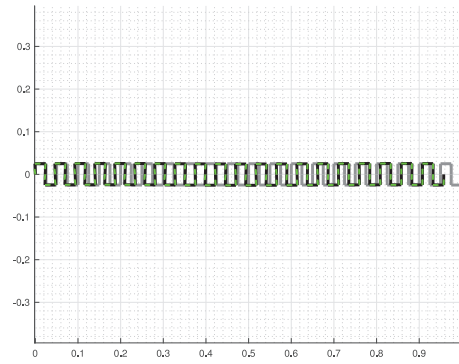
After this preliminary analysis, the application of a compression force, exhibiting a linear time evolution law with slope  $\dot{p} = -8$  N/s, is considered. Figure 4 shows the displacement evolution and the phase portrait (velocity vs. displacement) for the horizontal displacement and the cross-section rotation of the right end of the duoskelion structure.<sup>3</sup> Figure 5 is a stroboscopic image of the motion of the duoskelion structure.<sup>4</sup>

Both Figures 4 and 5 are useful in illustrating the mechanical behavior of the considered simply supported duoskelion beam-like structure subjected to a compression load. Looking at Figure 4, it can be seen that, after some small initial vibrations, there is a sudden buckling and the slope of the displacement increases rapidly. Looking at Figure 5, it is possible to notice that the initial vibrations are mainly due to an extensional deformation mode and that, following buckling, the first (bending) mode is activated, at least initially. It is worth remarking that no imperfection at all has been utilized, as is customarily the case when dealing with the classic Euler–Bernoulli beam theory. Indeed, the duoskelion geometry, which is a so-called chiral one, determines a preferential buckling direction that allows any indeterminacy occurring before the post-buckling equilibrium path to be overcome naturally. It is, in fact, evident that the duoskelion structure shows some characteristic symmetry properties that play a role in its overall behavior. Indeed, while the geometry of the undeformed duoskelion structure is invariant on  $\pm 180^\circ$  rotations, it is not invariant as such when reflected with respect to its axial ( $x$ ) and transverse ( $y$ ) axes. This is why the duoskelion beam is considered to be a chiral structure. Clearly, beams with opposite chirality, obtainable one from the other by reflection, might be considered. Opposite chiralities obviously affect the overall behavior of the beam differently, with the different results relatable by specific symmetries.

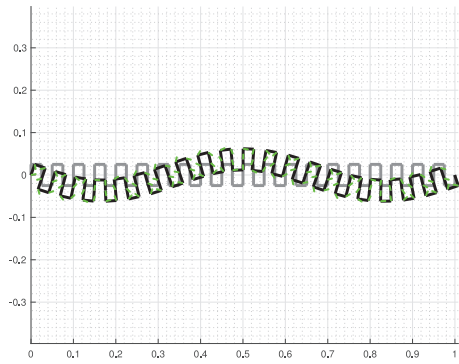




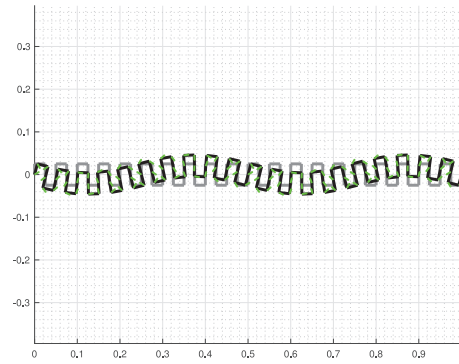
(a)  $T_1 = 0.9063$  s



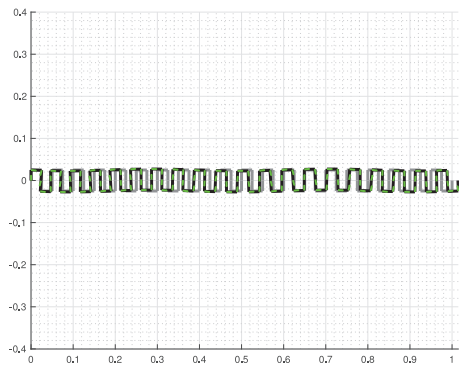
(b)  $T_2 = 0.2279$  s



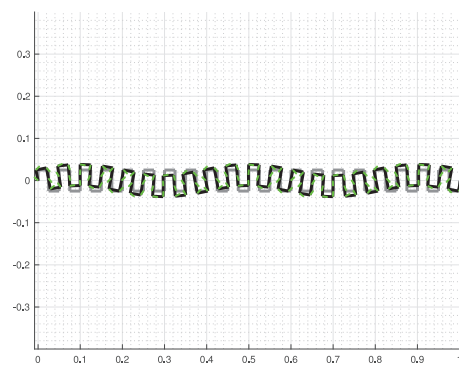
(c)  $T_3 = 0.1161$  s



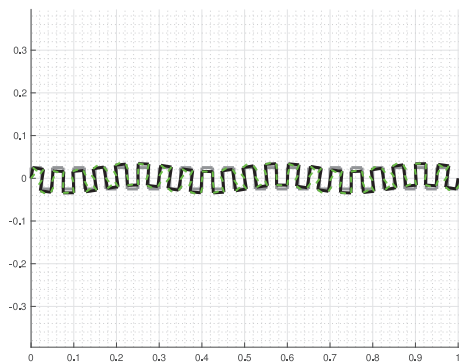
(d)  $T_4 = 0.1024$  s



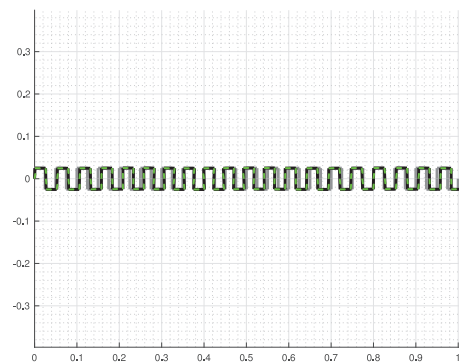
(e)  $T_5 = 0.05840$  s



(f)  $T_6 = 0.03878$  s



(g)  $T_7 = 0.03803$  s



(h)  $T_8 = 0.02610$  s

**Figure 3.** Simply supported duoskelion structure with 20 cells. First eight natural modes and periods.

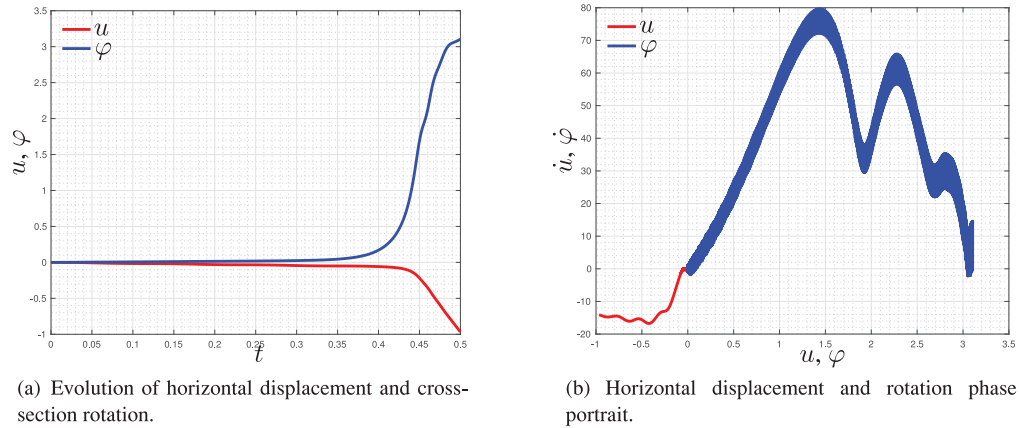


**Figure 4.** Simply supported duoskelion structure with 20 cells: (a) evolution of the horizontal displacement and rotation of the cross-section of the right end; (b) corresponding phase portrait. Red lines: horizontal displacement; blue lines: cross-section rotation.

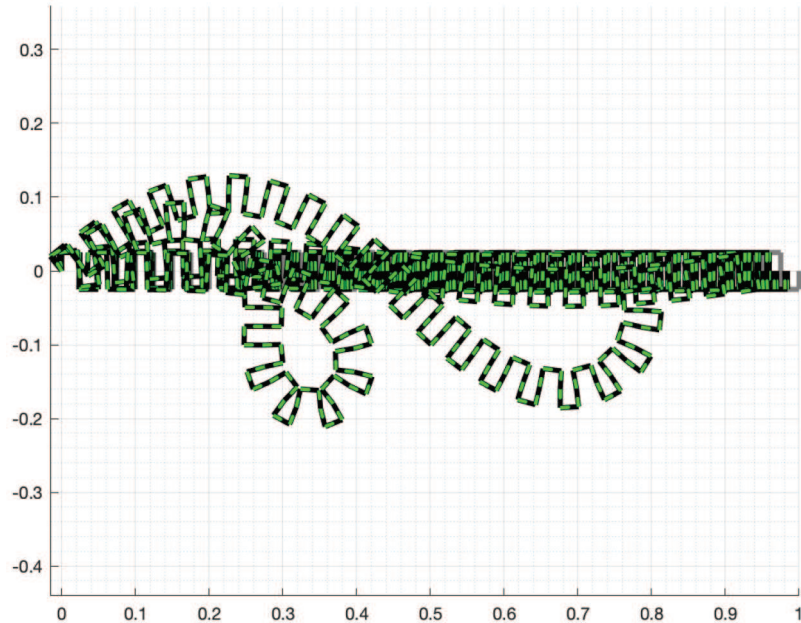


**Figure 5.** Stroboscopic representation of the evolution of the current configuration of the simply supported duoskelion structure subjected to a compression load.

We now address the second test, which is characterized by different end conditions. More precisely, the left end is clamped and rotation of the right end is prevented, as well as its vertical displacement, i.e. the right end is constrained with a sliding joint. Once again, a modal analysis is performed to compute the natural periods in the reference configuration. Figure 6 shows the first eight natural modes and periods. The last period is  $T_n = 4.952 \times 10^{-7}$  s. Of the natural modes shown in Figure 6, two extensional modes, the third and the sixth modes, can be identified. The remaining six modes are bending modes.

As before, following the modal analysis, the application on the right end of a compression force is considered. Again, the compression force evolves linearly with time and its slope is equal to  $\dot{p} = -8$  N/s. Figure 7 shows the displacement evolution and the phase portrait (velocity vs. displacement) for the horizontal displacement and the cross-section rotation of the right end of the duoskelion beam. Figure 8 shows a stroboscopic image of the motion of the duoskelion structure.<sup>5</sup>

As for the previous test, both Figures 7 and 8 are useful in illustrating the mechanical behavior of the considered simply supported duoskelion beam-like structure subjected to a compression load. Looking at Figure 7, it can be seen that, after some small initial vibrations, there is a sudden buckling and the slope of the displacement

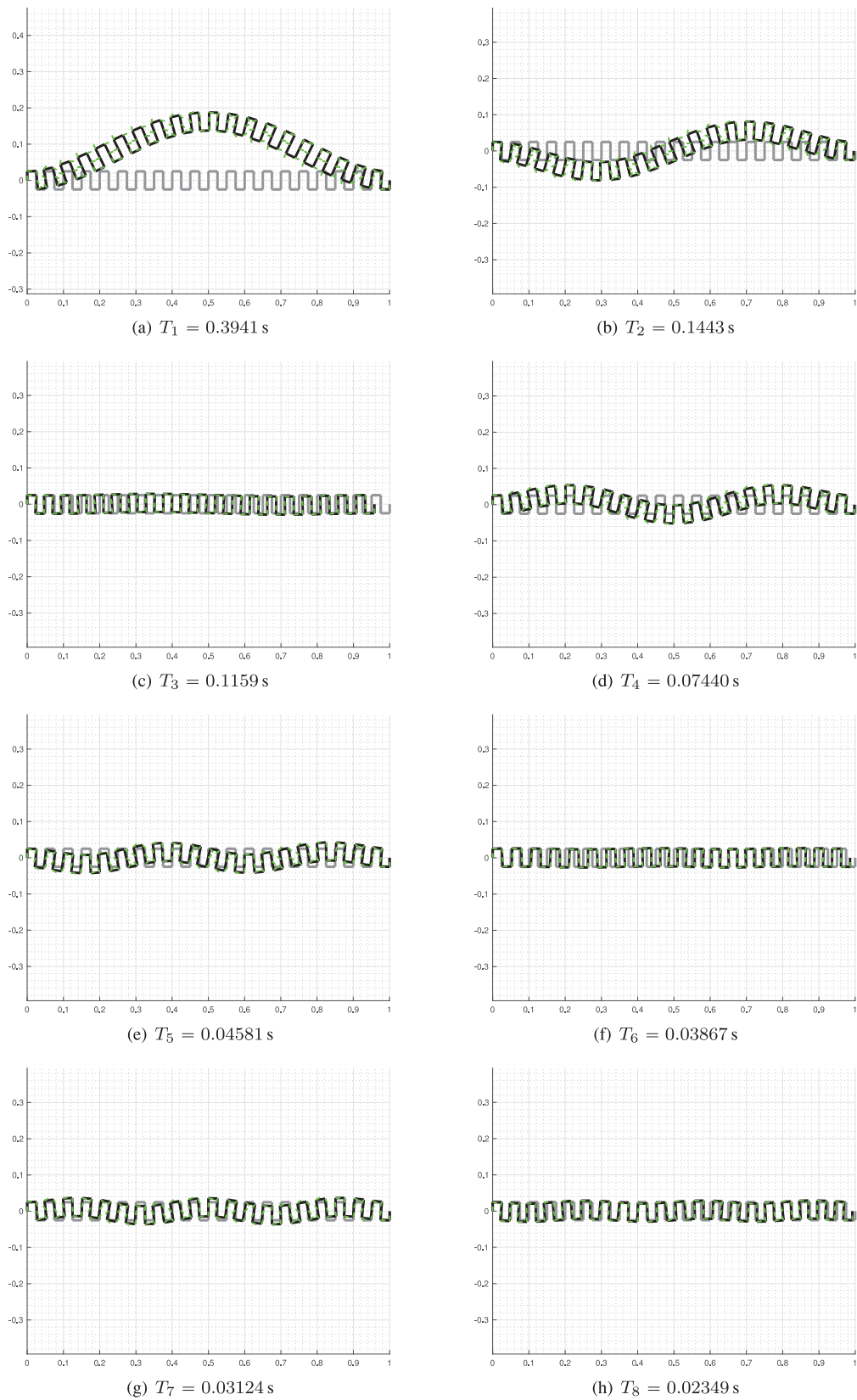


**Figure 6.** Duoskelion structure with 20 unit cells and clamp–sliding joint conditions. First eight natural modes and periods.

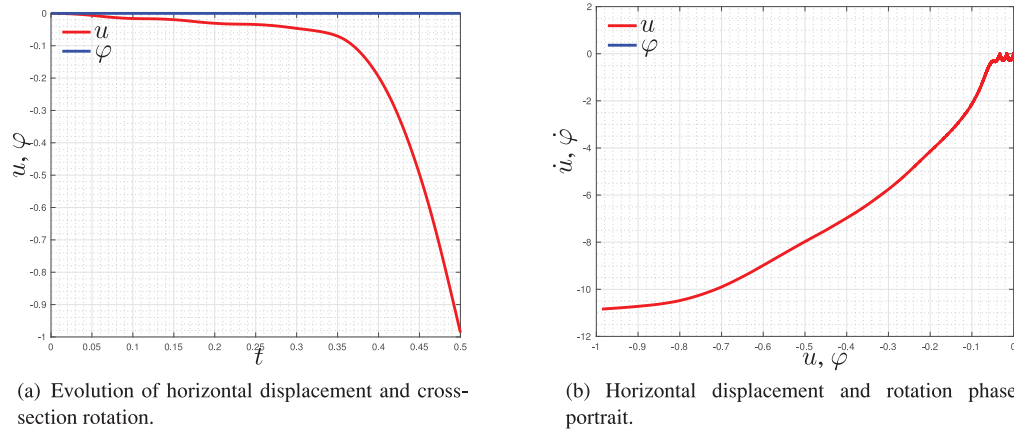


**Figure 7.** Duoskelion structure with 20 unit cells and clamp–sliding joint conditions: (a) evolution of the horizontal displacement and rotation of the cross-section of the right end; (b) corresponding phase portrait. Red lines: horizontal displacement; blue lines: cross-section rotation.

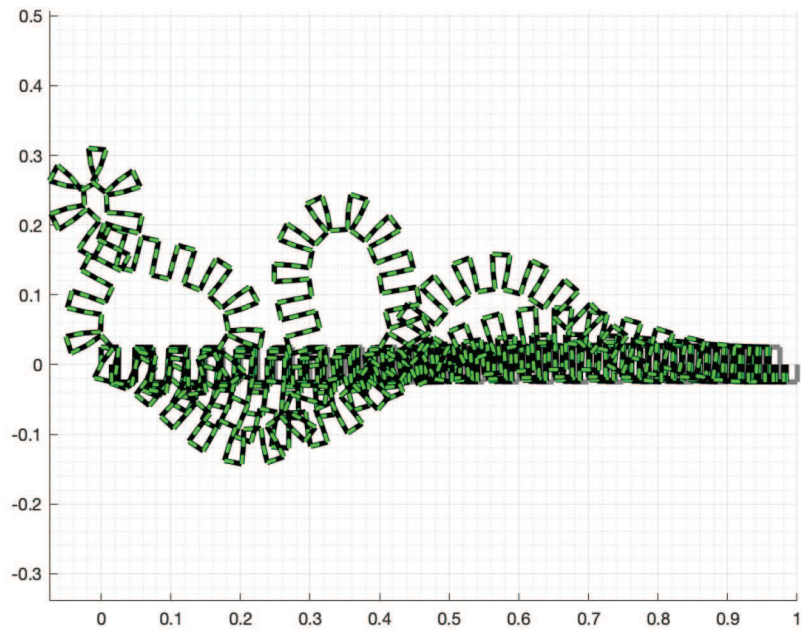
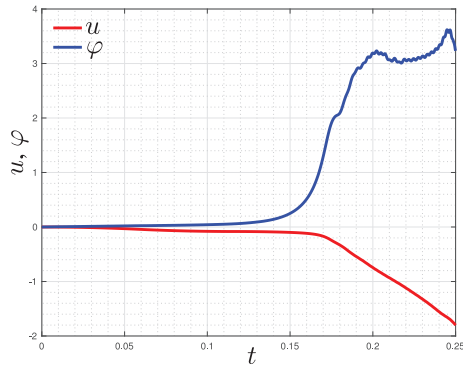


**Figure 8.** Duoskelion structure with 20 unit cells and clamp–sliding joint conditions. Stroboscopic representation of the evolution of the current configuration of the duoskelion structure subjected to a compression load.

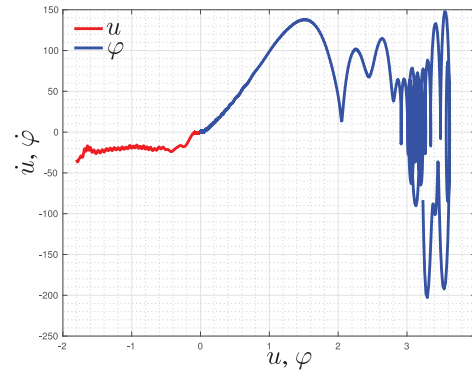
increases rapidly. Looking at Figure 8, it is possible to notice that the initial vibrations are mainly due to an extensional deformation mode and that, following buckling, the second (bending) mode is activated, at least initially. Again, no imperfection at all has been utilized to compute the post-buckling equilibrium path, as is customarily the case when dealing with the classic Euler–Bernoulli beam theory.

### 3.3. Influence of the loading rate

The numerical simulations described in the foregoing sections were repeated considering a different loading rate: a fast compression force at the right end. With this aim, the slope of the force evolution in time was set at  $\dot{p} = -40$  N/s.



(a) Evolution of horizontal displacement and cross-section rotation.



(b) Horizontal displacement and rotation phase portrait.

**Figure 9.** Simply supported duoskelion structure with 20 unit cells subjected to a fast compression load: (a) evolution of the horizontal displacement and rotation of the cross-section of the right end; (b) corresponding phase portrait. Red lines: horizontal displacement; blue lines: cross-section rotation.

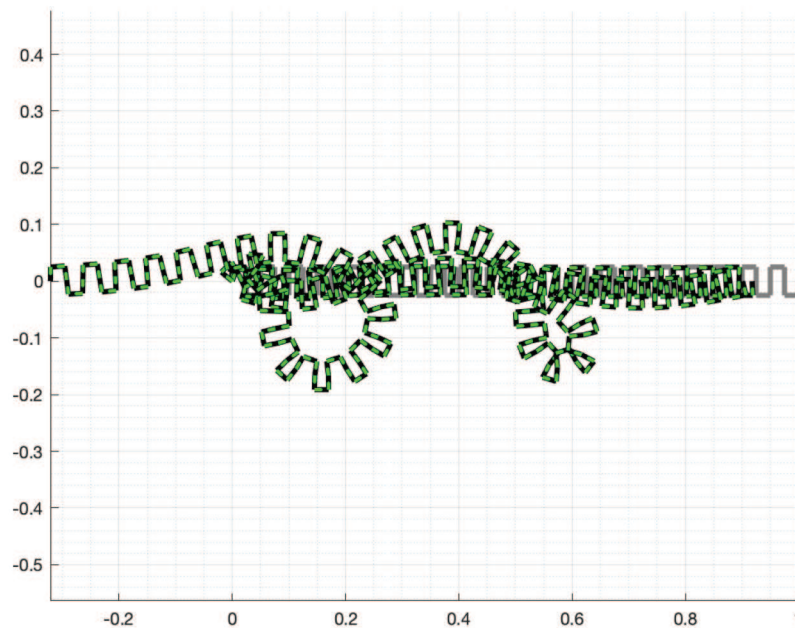
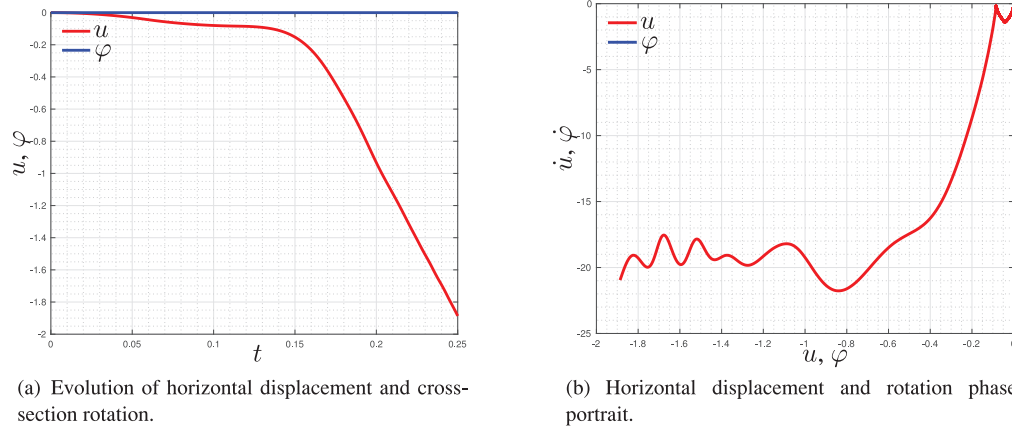


**Figure 10.** Simply supported duoskelion structure with 20 unit cells. Stroboscopic representation of the evolution of the current configuration of the duoskelion structure subjected to a fast compression load.

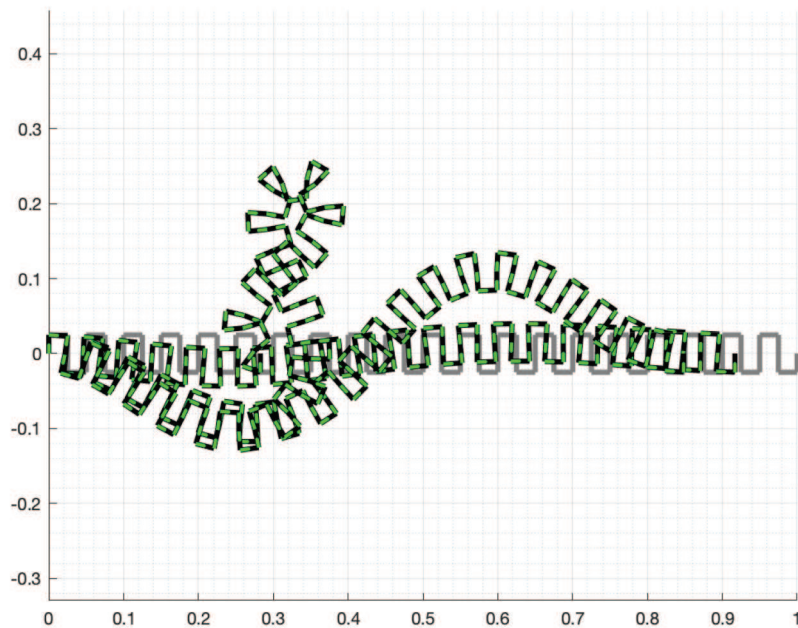
Let us first consider the case of simply supported end conditions. Clearly, as only the applied force is changing—only its magnitude, actually—the modal analysis in Figure 3 is still valid. Figure 9 shows the displacement evolution and the phase portrait (velocity vs. displacement) for the horizontal displacement and the cross-section rotation of the right end of the duoskelion structure.

Figure 10 shows a stroboscopic image of the motion of the duoskelion structure.<sup>6</sup> As for the previously reported cases, Figures 9 and 10 show that, after some small initial vibrations, there is a sudden buckling and the slope of the displacement increases rapidly. Looking at Figure 10, it is possible to notice that the initial vibrations are mainly due to an extensional deformation mode and that, following buckling, the second (bending) mode is activated, at least initially.

Let us now consider the case of clamped–sliding joint end conditions. Again, as only the applied force is changing with respect to the previously addressed case with clamped–sliding joint conditions—only its magnitude, actually—the modal analysis in Figure 6 is still valid. Figure 11 shows the displacement evolution and the



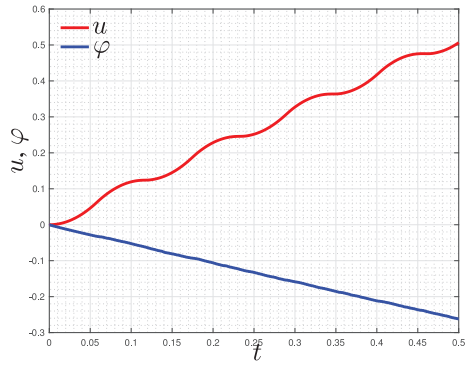
**Figure 11.** Duoskelion structure with 20 unit cells and clamp–sliding joint end conditions subjected to a fast compression load: (a) evolution of the horizontal displacement and rotation of the cross-section of the right end; (b) corresponding phase portrait. Red lines: horizontal displacement; blue lines: cross-section rotation.



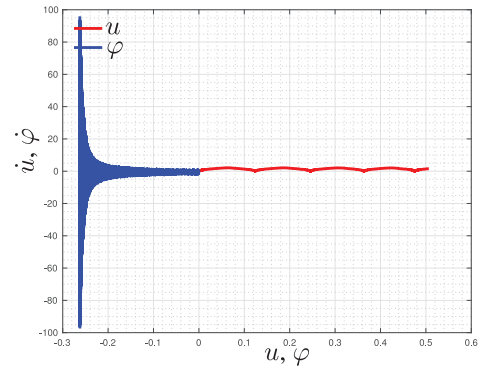
**Figure 12.** Duoskelion structure with 20 unit cells with clamp–sliding joint end conditions. Stroboscopic representation of the evolution of the current configuration of the duoskelion structure subjected to a fast compression load.

phase portrait (velocity vs. displacement) for the horizontal displacement and the cross-section rotation of the right end of the duoskelion structure.

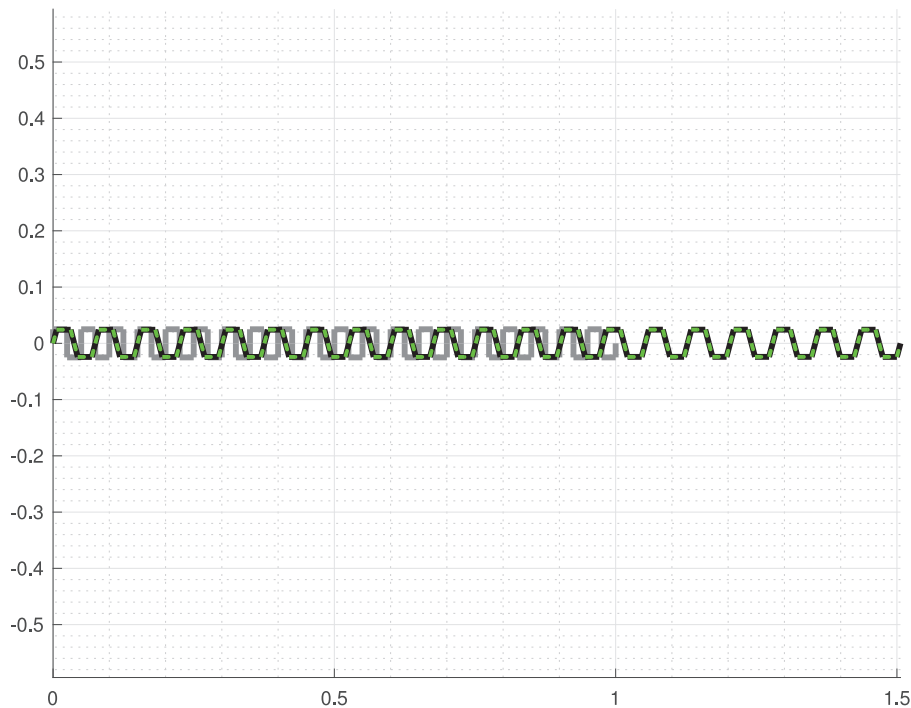
Figure 12 shows a stroboscopic image of the motion of the duoskelion structure.<sup>7</sup> As for the previously reported cases, Figures 11 and 12 show that, after some small initial vibrations, there is a sudden buckling and the slope of the displacement increases rapidly. Looking at Figure 12, it is possible to notice that the initial vibrations are mainly due to an extensional deformation mode and that, following buckling, the first (bending) mode is activated, at least initially.



(a) Evolution of horizontal displacement and cross-section rotation.



(b) Horizontal displacement and rotation phase portrait.



(c) Final configuration.

**Figure 13.** Duoskelion structure with 20 unit cells and simply supported end conditions subjected to a traction load: (a) evolution of the horizontal displacement and rotation of the cross-section of the right end; (b) corresponding phase portrait; (c) final configuration. Red lines: horizontal displacement; blue lines: cross-section rotation.

### 3.4. Traction test

In this subsection, a traction test is considered for both simply supported and clamp–sliding joint end conditions. A traction load is applied to the right end of the structure. As before, such a load is varied linearly with time and its slope is  $\dot{p} = 60 \text{ N/s}$ .

Let us first consider the simply supported end conditions. Clearly, as only the applied force is changing—only its magnitude, actually—the modal analysis in Figure 3 still holds valid. Figure 13(a) and (b) show, respectively, the displacement evolution and the phase portrait (velocity vs. displacement) for the horizontal displacement and the cross-section rotation of the right end of the duoskelion structure. Figure 13(c) shows the final configuration.

Let us now consider the clamp–sliding joint end conditions. Again, as only the applied force is changing—only its magnitude, actually—the modal analysis in Figure 6 still holds valid. Similarly to the previous case,

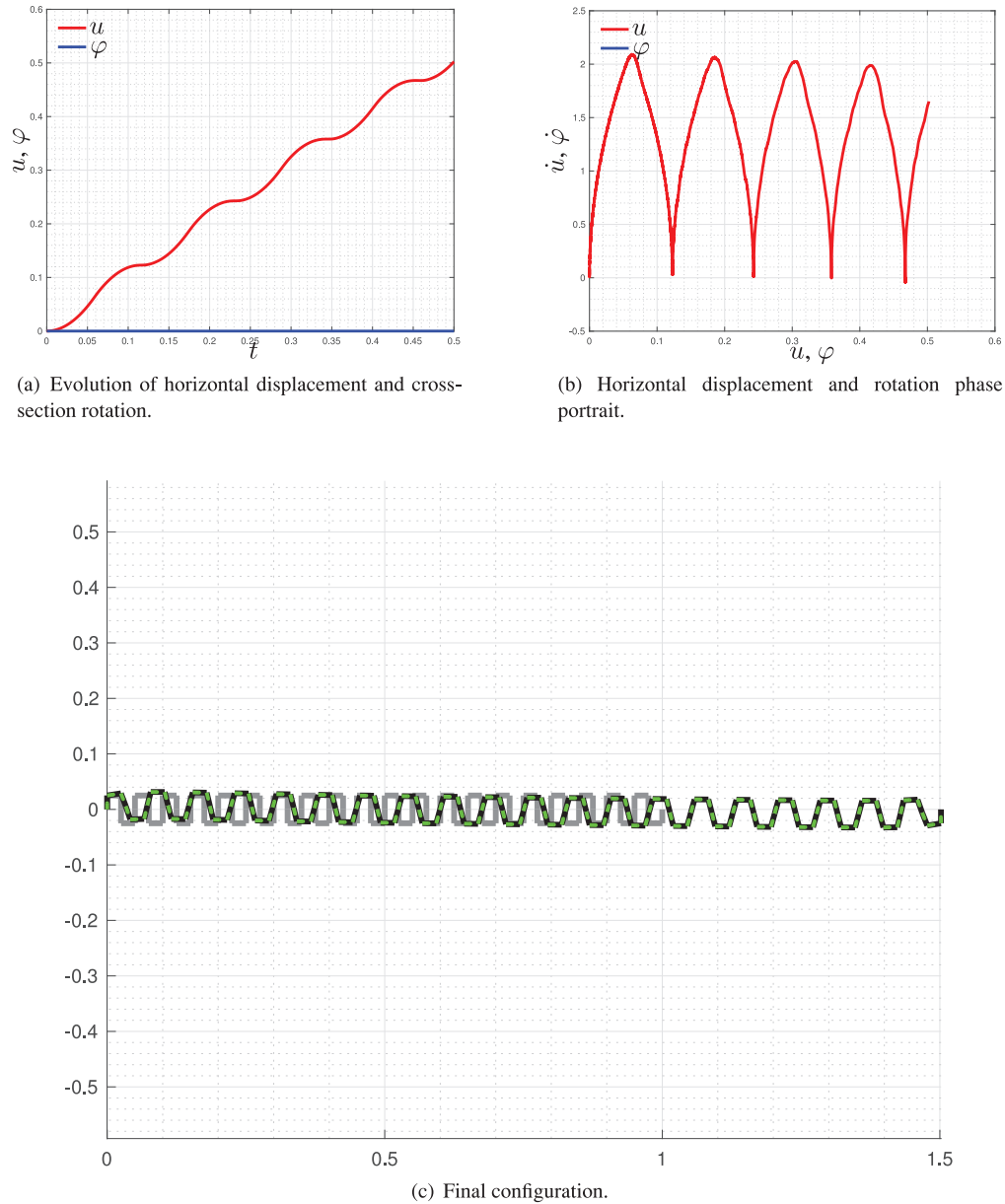


**Figure 14.** Duoskelion structure with 20 unit cells and clamp–sliding joint end conditions subjected to a traction load: (a) evolution of the horizontal displacement and rotation of the cross-section of the right end; (b) corresponding phase portrait; (c) final configuration. Red lines: horizontal displacement; blue lines: cross-section rotation.

Figure 14(a) and (b) show, respectively, the displacement evolution and the phase portrait (velocity vs. displacement) for the horizontal displacement and the cross-section rotation of the right end of the duoskelion structure. Figure 14(c) shows the final configuration.

Clearly, in the simply supported case, no significant displacement in the vertical direction is observed. Therefore, the duoskelion structure is deforming only through an extensional mode. The deformation is mainly concentrated at the nodes between horizontal and vertical tracts in the form of bending. The horizontal displacement of the right end increases in an almost linear manner. Unexpectedly, the rotation at the right end oscillates with increasing amplitude and velocity. More particularly, the velocity increases superlinearly. In the case of clamp–sliding end conditions, vertical displacement is instead noticeable, even if almost negligible.



**Table 2.** Simply supported duoskelion structure. Natural periods, in seconds, for different stiffness datasets.

Case	$T_1$	$T_2$	$T_3$	$T_4$	$T_5$	$T_6$	$T_7$	$T_8$	$T_n$
Reference	0.9063	0.2279	0.1161	0.1024	0.05840	0.03878	0.03803	0.02610	$4.952 \times 10^{-7}$
$c \rightarrow \infty$	0.9032	0.2279	0.1160	0.1024	0.05839	0.03877	0.03802	0.02610	$4.957 \times 10^{-10}$
$a, c \rightarrow \infty$	0.9013	0.2279	0.1160	0.1024	0.05839	0.03877	0.03802	0.02700	$4.957 \times 10^{-10}$

### 3.5. Analysis of the sensitivity to stiffness parameters

The sensitivity analysis has as its main objective, an assessment of the influence of the stiffness parameters  $a$  and  $c$  on the dynamic behavior of the duoskelion structure, with 20 cells analyzed until now. Specifically, the simply supported case is considered, with two cases of particular interest (as an example, see [79, 80]): (i)  $c \rightarrow \infty$ , i.e. equivalent to neglecting shear deformability; (ii)  $c \rightarrow \infty$  and  $a \rightarrow \infty$ , i.e. equivalent to neglecting both shear and extensional deformabilities.

Departing from the values of  $a$  and  $c$  reported in Table 1, the case  $c_\infty = 10^6 \times c$  was first considered and, successively, the cases  $a_\infty = 10^6 \times a$  and  $c_\infty = 10^6 \times c$  were considered. By making use of these datasets, we recalculated natural modes and periods in the reference configuration. The first eight natural periods and the last natural period  $T_n$  are given in Table 2 for the considered study cases, along with those obtained for the reference dataset. Only the first and last natural periods are necessary to initialize Casciaro's integration scheme, but a comparison of the values assumed by the first set of modes is useful. We first observe that no relevant change in the first eight natural modes occurs, although these have not been reported in the paper, and that the periods also change in a very limited way. More specifically, we observe a very limited change in the periods of the first, bending, mode and the eighth, extensional, mode: 0.55% for the first mode and 3.4% for the eighth mode, for the case  $a$  and  $c \rightarrow \infty$ .

We also conducted the numerical simulation reported in the foregoing relative to a compression force varying with a linear evolution law and slope  $\dot{p} = -8$  N/s for both  $c \rightarrow \infty$  and  $a, c \rightarrow \infty$ . No relevant changes are observed in the response, even though a smaller value of the time step is required to perform the time integration. This derives from a greater ill-conditioning for the nonlinear system of equations to integrate.

## 4. Concluding remarks and future challenges

In this study, we have recalled the formulation of a recently proposed nonlinear discrete beam element capable of taking into account shearing deformation, on which we base the entire analysis. Such a beam element is introduced in the general three-dimensional setting, and its kinematics and strain and kinetic energies are defined. After having recalled the formulation of the discrete beam element, realistic values of the model parameters are found by making use of the Saint-Venant formulas. We then report on the numerical simulations performed for a duoskelion structure, based on the previously introduced discrete beam element, using Casciaro's time integration scheme. Specifically, results illustrating the dynamic buckling of beam-like duoskelion structures for different end conditions are presented, as well as results concerning the influence of the loading velocity and stiffness parameters on the observed mechanical behaviors. It is concluded that, owing to their chirality, duoskelion structures present an exotic behavior, especially at large strain, that deserves to be further studied. It is believed that this study will contribute to the understanding of their mechanical behavior and will present a useful tool for validating an asymptotic homogenization process for the nonlinear dynamics of duoskelion structures, which is currently under study.

### Notes


- Let us remember that the axial vector  $\mathbf{w}$  of a skew symmetric second-order tensor  $\mathbf{C}$  is defined by the relationship  $\mathbf{C}\mathbf{v} = \mathbf{w} \times \mathbf{v}$ , where  $\times$  is the cross-product between two vectors. In an orthonormal basis having the same orientation of the space,  $\mathbf{w} \times \mathbf{v}$  is given by the pseudotensorial formula  $\varepsilon_{ijk} w^i v^j$ , where  $\varepsilon_{ijk}$  is the Levi-Civita symbol, defined as

$$\varepsilon_{ijk} = \begin{cases} +1 & \text{if } (i, j, k) \text{ is } (1, 2, 3), (2, 3, 1), \text{ or } (3, 1, 2), \\ -1 & \text{if } (i, j, k) \text{ is } (3, 2, 1), (1, 3, 2), \text{ or } (2, 1, 3), \\ 0 & \text{if } i = j, \text{ or } j = k, \text{ or } k = i. \end{cases}$$

The vectorial invariant of an orthogonal tensor  $\mathbf{R}$ , which is not—generally speaking—skew symmetric, is defined as the axial vector of the tensor  $\mathbf{R} - \mathbf{R}^T$ . There is an interesting interpretation of the vectorial invariant of an orthogonal tensor  $\mathbf{R}$ . Given a rotation tensor  $\mathbf{R}$ , a vector  $\mathbf{a}$  parallel to the rotation axis must satisfy  $\mathbf{R}\mathbf{a} = \mathbf{a}$ . This equation admits, up to a scalar factor, a unique solution  $\mathbf{a}$ , unless  $\mathbf{R} = \mathbf{I}$ . The vector  $\mathbf{a}$  belongs to the null space of  $\mathbf{R} - \mathbf{I}$  or, equivalently, is an eigenvector of  $\mathbf{R}$  associated to the eigenvalue  $+1$ . The vector  $\mathbf{a}$ , if  $\mathbf{R} - \mathbf{R}^T$  is different from the null tensor  $\mathbf{0}$ , i.e.  $\mathbf{R}$  is not symmetric, can also be found considering that  $(\mathbf{R} - \mathbf{R}^T)\mathbf{a} = \mathbf{0}$ . Since  $\mathbf{R} - \mathbf{R}^T$  is skew symmetric—actually, it is equal to twice the skew symmetric part of  $\mathbf{R}$ —we can define the axial vector  $\mathbf{w}$  of the tensor  $\mathbf{R} - \mathbf{R}^T$ , namely its vectorial invariant. Hence, we have  $\mathbf{w} \times \mathbf{a} = \mathbf{0}$ , which means that  $\mathbf{w}$  and  $\mathbf{a}$ , the rotation axis of  $\mathbf{R}$ , are parallel.

2. Since  $\mathbf{Q}$  is an orthogonal tensor, we have  $\mathbf{Q}^T\mathbf{Q} = \mathbf{I}$ . Therefore, deriving both sides of this equality with respect to the time variable  $t$ , we get  $d(\mathbf{Q}^T\mathbf{Q})/dt = \dot{\mathbf{Q}}^T\mathbf{Q} + \mathbf{Q}^T\dot{\mathbf{Q}} = \mathbf{0}$ . As a consequence, we have that  $(\dot{\mathbf{Q}}^T\mathbf{Q})^T = -\dot{\mathbf{Q}}^T\mathbf{Q}$ .
3. All the rotations considered in this work are expressed in radians.
4. A short movie showing the motion of the considered duoskelion structure is available as supplementary material associated with this work, see the file `duoskelion20ss_slow_dynamicload.avi`.
5. A short movie showing the motion of the considered duoskelion structure is available as supplementary material associated with this work, see the file `duoskelion20cc_slow_dynamicload.avi`.
6. A short movie showing the motion of the considered duoskelion structure is available as supplementary material associated with this work, see the file `duoskelion20ss_fast_dynamicload.avi`.
7. A short movie showing the motion of the considered duoskelion structure is available as supplementary material associated with this work, see the file `duoskelion20cc_fast_dynamicload.avi`.

## ORCID iD

Emilio Turco  <https://orcid.org/0000-0002-8263-7034>

## References

- [1] Barchiesi, E, Spagnuolo, M, and Placidi, L. Mechanical metamaterials: A state of the art. *Math Mech Solids* 2019; 24(1): 212–234.
- [2] di Cosmo, F, Laudato, M, and Spagnuolo, M. Acoustic metamaterials based on local resonances: Homogenization, optimization and applications. In: Altenbach, H, Pouget, J, Rousseau, M, et al. (eds.) *Generalized models and non-classical approaches in complex materials I*. Cham: Springer International, 2018, 247–274.
- [3] Barchiesi, E, Di Cosmo, F, and Laudato, M. A review of some selected examples of mechanical and acoustic metamaterials. In: dell’Isola, F and Steigmann, DJ (eds.) *Discrete and continuum models for complex metamaterials*. Cambridge: Cambridge University Press, 2020, 52–102.
- [4] Eremeyev, VA, and Turco, E. Enriched buckling for beam-lattice metamaterials. *Mech Res Commun* 2020; 103: 103458.
- [5] Cazzani, A, Malagù, M, and Turco, E. Isogeometric analysis of plane curved beams. *Math Mech Solids* 2016; 21(5): 562–577.
- [6] Cazzani, A, Malagù, M, Turco, E, et al. Constitutive models for strongly curved beams in the frame of isogeometric analysis. *Math Mech Solids* 2016; 21(2): 182–209.
- [7] Lurie, S, and Solyaev, Y. On the formulation of elastic and electroelastic gradient beam theories. *Continuum Mech Thermodyn* 2019; 31(6): 1601–1613.
- [8] Harsch, J, Capobianco, G, and Eugster, SR. Finite element formulations for constrained spatial nonlinear beam theories. *Math Mech Solids*. Epub ahead of print 27 April 2021. DOI: 10.1177/10812865211000790.
- [9] Eugster, SR, Hesch, C, Betsch, P, et al. Director-based beam finite elements relying on the geometrically exact beam theory formulated in skew coordinates. *Int J Numer Methods Eng* 2014; 97(2): 111–129.
- [10] Harsch, J, and Eugster, SR. Finite element analysis of planar nonlinear classical beam theories. In: Abali, BE and Giorgio, I (eds.) *Developments and novel approaches in nonlinear solid body mechanics*. Cham: Springer, 2020, 123–157.
- [11] Eugster, SR, and Harsch, J. A variational formulation of classical nonlinear beam theories. In: Abali, BE and Giorgio, I (eds.) *Developments and novel approaches in nonlinear solid body mechanics*. Cham: Springer, 2020, 95–121.
- [12] Giorgio, I. A discrete formulation of Kirchhoff rods in large-motion dynamics. *Math Mech Solids* 2020; 25(5): 1081–1100.

- 
- [13] Solyaev, Y, Lurie, S, Koshurina, A, et al. On a combined thermal/mechanical performance of a foam-filled sandwich panels. *Int J Eng Sci* 2019; 134: 66–76.
- [14] Solyaev, Y, and Lurie, S. Pure bending of a piezoelectric layer in second gradient electroelasticity theory. *Acta Mech* 2019; 230(12): 4197–4211.
- [15] dell’Isola, F, and Steigmann, D. A two-dimensional gradient-elasticity theory for woven fabrics. *J Elast* 2015; 118(1): 113–125.
- [16] dell’Isola, F, Giorgio, I, Pawlikowski, M, et al. Large deformations of planar extensible beams and pantographic lattices: Heuristic homogenisation, experimental and numerical examples of equilibrium. *Proc R Soc London, Ser A* 2016; 472(2185): 20150790.
- [17] Altenbach, J, Altenbach, H, and Eremeyev, VA. On generalized Cosserat-type theories of plates and shells: A short review and bibliography. *Arch Appl Mech* 2010; 80(1): 73–92.
- [18] Altenbach, H, and Eremeyev, VA. On the shell theory on the nanoscale with surface stresses. *Int J Eng Sci* 2011; 49(12): 1294–1301.
- [19] Scerrato, D, Giorgio, I, and Rizzi, NL. Three-dimensional instabilities of pantographic sheets with parabolic lattices: Numerical investigations. *Z Angew Math Mech* 2016; 67: 53.
- [20] Giorgio, I, Grygoruk, R, dell’Isola, F, et al. Pattern formation in the three-dimensional deformations of fibered sheets. *Mech Res Commun* 2015; 69: 164–171.
- [21] Giorgio, I. Lattice shells composed of two families of curved Kirchhoff rods: An archetypal example, topology optimization of a cycloidal metamaterial. *Continuum Mech Thermodyn* 2021; 33(4): 1063–1082.
- [22] Berezovski, A, Giorgio, I, and Della Corte, A. Interfaces in micromorphic materials: Wave transmission and reflection with numerical simulations. *Math Mech Solids* 2016; 21(1): 37–51.
- [23] Reiher, JC, Giorgio, I, and Bertram, A. Finite-element analysis of polyhedra under point and line forces in second-strain gradient elasticity. *J Eng Mech* 2017; 143(2): 04016112.
- [24] Yang, H, Ganzosch, G, Giorgio, I, et al. Material characterization and computations of a polymeric metamaterial with a pantographic substructure. *Z Angew Math Phys* 2018; 69(4): 105.
- [25] Barchiesi, E, Eugster, SR, Placidi, L, et al. Pantographic beam: A complete second gradient 1D-continuum in plane. *Z Angew Math Phys* 2019; 70: 135.
- [26] Placidi, L, Andreaus, U, and Giorgio, I. Identification of two-dimensional pantographic structure via a linear D4 orthotropic second gradient elastic model. *J Eng Math* 2017; 103(1): 1–21.
- [27] Giorgio, I, Rizzi, NL, and Turco, E. Continuum modelling of pantographic sheets for out-of-plane bifurcation and vibrational analysis. *Proc R Soc London, Ser A* 2017; 473(2207): 20170636.
- [28] Giorgio, I, Della Corte, A, and dell’Isola, F. Dynamics of 1D nonlinear pantographic continua. *Nonlinear Dyn* 2017; 88(1): 21–31.
- [29] dell’Isola, F, Della Corte, A, and Giorgio, I. Higher gradient continua: The legacy of Piola, Mindlin, Sedov and Toupin and some future research perspectives. *Math Mech Solids* 2017; 22(4): 852–872.
- [30] Abali, BEA, Müller, WH, and dell’Isola, F. Theory and computation of higher gradient elasticity theories based on action principles. *Arch Appl Mech* 2017; 87(9): 1495–1510.
- [31] Javili, A, dell’Isola, F, and Steinmann, P. Geometrically nonlinear higher-gradient elasticity with energetic boundaries. *J Mech Phys Solids* 2013; 61(12): 2381–2401.
- [32] Misra, A, Placidi, L, dell’Isola, F, et al. Identification of a geometrically nonlinear micromorphic continuum via granular micromechanics. *Z Ang Math Phys* 2021; 72(4): 157.
- [33] Giorgio, I, De Angelo, M, Turco, E, et al. A Biot–Cosserat two-dimensional elastic nonlinear model for a micromorphic medium. *Continuum Mech Thermodyn* 2020; 32: 1357–1369.
- [34] Giorgio, I, dell’Isola, F, and Misra, A. Chirality in 2D Cosserat media related to stretch-micro-rotation coupling with links to granular micromechanics. *Int J Solids Struct* 2020; 202: 28–38.
- [35] Altenbach, H, and Eremeyev, VA. On the linear theory of micropolar plates. *Z Angew Math Mech* 2009; 89(4): 242–256.
- [36] dell’Isola, F, Andreaus, U, and Placidi, L. At the origins and in the vanguard of peridynamics, non-local and higher-gradient continuum mechanics: An underestimated and still topical contribution of Gabrio Piola. *Math Mech Solids* 2015; 20(8): 887–928.
- [37] Danesh, H, Javanbakhtand, M, and Aghdam, MM. A comparative study of 1D nonlocal integral Timoshenko beam and 2D nonlocal integral elasticity theories for bending of nanoscale beams. *Continuum Mech Thermodyn*. Epub ahead of print 25 February 2021. DOI: 10.1007/s00161-021-00976-7.
- [38] Danesh, H, Javanbakhtand, M, Barchiesi, E, et al. Coupled phase field and nonlocal integral elasticity analysis of stress-induced martensitic transformations at the nanoscale: boundary effects, limitations and contradictions. *Continuum Mech Thermodyn*. Epub ahead of print 23 July 2021. DOI: 10.1007/s00161-021-01042-y.
- [39] Danesh, H, and Javanbakhtand, M. Free vibration analysis of nonlocal nanobeams: A comparison of the one-dimensional nonlocal integral Timoshenko beam theory with the two-dimensional nonlocal integral elasticity theory. *Math Mech Solids*. Epub ahead of print 24 July 2021. DOI: 10.1177/10812865211031278.
- [40] Turco, E, dell’Isola, F, Cazzani, A, et al. Hencky-type discrete model for pantographic structures: Numerical comparison with second gradient continuum models. *Z Angew Math Phys* 2016; 67: 85.
- [41] Cazzani, A, Serra, M, Stochino, F, et al. A refined assumed strain finite element model for statics and dynamics of laminated plates. *Continuum Mech Thermodyn* 2020; 32(3): 665–692.

- [42] Baroudi, D, Giorgio, I, Battista, A, et al. Nonlinear dynamics of uniformly loaded elastica: Experimental and numerical evidence of motion around curled stable equilibrium configurations. *Z Angew Math Mech* 2019; 99(7): e201800121.
- [43] Bilotta, A, Morassi, A, and Turco, E. The use of quasi-isospectral operators for damage detection in rods. *Meccanica* 2018; 53(1–2): 319–345.
- [44] Placidi, L, and Barchiesi, E. Energy approach to brittle fracture in strain-gradient modelling. *Proc R Soc London, Ser A* 2018; 474(2210): 20170878.
- [45] Greco, L. An iso-parametric  $G^1$ -conforming finite element for the nonlinear analysis of Kirchhoff rod. Part I: The 2D case. *Continuum Mech Thermodyn* 2020; 32: 1473–1496.
- [46] Barchiesi, E, dell’Isola, F, Hild, F, et al. Two-dimensional continua capable of large elastic extension in two independent directions: Asymptotic homogenization, numerical simulations and experimental evidence. *Mech Res Commun* 2020; 103: 103466.
- [47] Barchiesi, E, Eugster, SR, dell’Isola, F, et al. Large in-plane elastic deformations of bi-pantographic fabrics: Asymptotic homogenization and experimental validation. *Math Mech Solids* 2020; 25(3): 739–767.
- [48] Yang, H, and Müller, WH. Size effects of mechanical metamaterials: A computational study based on a second-order asymptotic homogenization method. *Arch Appl Mech* 2021; 91(3): 1037–1053.
- [49] Rosi, G, Placidi, L, and Auffray, N. On the validity range of strain-gradient elasticity: A mixed static-dynamic identification procedure. *Eur J Mech A Solids* 2018; 69: 179–191.
- [50] Turco, E. Is the statistical approach suitable for identifying actions on structures? *Comput Struct* 2005; 83: 2112–2120.
- [51] De Angelo, M, Placidi, L, Nejjadsadeghi, N, et al. Non-standard Timoshenko beam model for chiral metamaterial: Identification of stiffness parameters. *Mech Res Commun* 2020; 103: 103462.
- [52] Barchiesi, E, Misra, A, Placidi, L, et al. Granular micromechanics-based identification of isotropic strain gradient parameters for elastic geometrically nonlinear deformations. *Z Angew Math Mech*. Epub ahead of print 28 May 2021. DOI: 10.1002/zamm.202100059.
- [53] Timofeev, D, Barchiesi, E, Misra, A, et al. Hemivariational continuum approach for granular solids with damage-induced anisotropy evolution. *Math Mech Solids* 2021; 26(5): 738–770.
- [54] Placidi, L, Barchiesi, E, Misra, A, et al. Micromechanics-based elasto-plastic–damage energy formulation for strain gradient solids with granular microstructure. *Continuum Mech Thermodyn*. 2021; 33: 2213–2241.
- [55] Barchiesi, E, dell’Isola, F, and Hild, F. On the validation of homogenized modeling for bi-pantographic metamaterials via digital image correlation. *Int J Solids Struct* 2021; 208: 49–62.
- [56] Barchiesi, E, Harsch, J, Ganzosch, G, et al. Discrete versus homogenized continuum modeling in finite deformation bias extension test of bi-pantographic fabrics. *Continuum Mech Thermodyn*. Epub ahead of print 12 September 2020. DOI: 10.1007/s00161-020-00917-w.
- [57] Yang, H, Abali, BE, Timofeev, D, et al. Determination of metamaterial parameters by means of a homogenization approach based on asymptotic analysis. *Continuum Mech Thermodyn* 2020; 32: 1251–1270.
- [58] Turco, E, Golaszewski, M, Cazzani, A, et al. Large deformations induced in planar pantographic sheets by loads applied on fibers: Experimental validation of a discrete Lagrangian model. *Mech Res Commun* 2016; 76: 51–56.
- [59] Turco, E, Golaszewski, M, Giorgio, I, et al. Pantographic lattices with non-orthogonal fibres: Experiments and their numerical simulations. *Composites, Part B* 2017; 118: 1–14.
- [60] Turco, E, Misra, A, Sarikaya, R, et al. Quantitative analysis of deformation mechanisms in pantographic substructures: Experiments and modeling. *Continuum Mech Thermodyn* 2019; 31(1): 209–223.
- [61] Ganzosch, G, dell’Isola, F, Turco, E, et al. Shearing tests applied to pantographic structures. *Acta Polytech CTU Proc* 2017; 7: 1–6.
- [62] Ciallella, A, Pasquali, D, Golaszewski, M, et al. A rate-independent internal friction to describe the hysteretic behavior of pantographic structures under cyclic loads. *Mech Res Commun* 2021; 116: 103761.
- [63] Turco, E, Barchiesi, E, and dell’Isola, F. A numerical investigation on impulse-induced nonlinear longitudinal waves in pantographic beams. *Math Mech Solids*. Epub ahead of print 5 May 2021. DOI: 10.1177/10812865211010877.
- [64] Turco, E. A numerical survey of nonlinear dynamical responses of discrete pantographic beams. *Continuum Mech Thermodyn* 2021; 33: 1465–1485.
- [65] dell’Isola, F, Seppacher, P, Spagnuolo, M, et al. Advances in pantographic structures: Design, manufacturing, models, experiments and image analyses. *Continuum Mech Thermodyn* 2019; 31(4): 1231–1282.
- [66] dell’Isola, F, Seppacher, P, Alibert, JJ, et al. Pantographic metamaterials: An example of mathematically driven design and of its technological challenges. *Continuum Mech Thermodyn* 2019; 31(4): 851–884.
- [67] Placidi, L, Greco, L, Bucci, S, et al. A second gradient formulation for a 2D fabric sheet with inextensible fibres. *Z Angew Math Phys* 2016; 67: 114.
- [68] Eremeyev, VA, dell’Isola, F, Boutin, C, et al. Linear pantographic sheets: Existence and uniqueness of weak solutions. *J Elast* 2018; 132(2): 175–196.
- [69] Hild, F, Misra, A, and dell’Isola, F. Multiscale DIC applied to pantographic structures. *Experimental Mechanics* 2021; 61(2): 431–443.
- [70] Auffray, N, Dirrenberger, J, and Rosi, G. A complete description of bi-dimensional anisotropic strain-gradient elasticity. *Int J Solids and Structures* 2015; 69: 195–206.

- 
- [71] Barchiesi, E, dell'Isola, F, Bersani, AM, et al. Equilibria determination of elastic articulated duoskelion beams in 2D via a Riks-type algorithm. *Int J Non Linear Mech* 2021; 128: 103628.
- [72] Turco, E. Discrete is it enough? The revival of Piola–Hencky keynotes to analyze three-dimensional *Elastica*. *Continuum Mech Thermodyn* 2018; 30(5): 1039–1057.
- [73] Turco, E, Barchiesi, E, Giorgio, I, et al. A Lagrangian Hencky-type non-linear model suitable for metamaterials design of shearable and extensible slender deformable bodies alternative to Timoshenko theory. *Int J Non Linear Mech* 2020; 123: 103481.
- [74] Elishakoff, I. Who developed the so-called Timoshenko beam theory? *Math Mech Solids* 2019; 25(1): 97–116.
- [75] Altenbach, H, Birsan, M, and Eremeyev, VA. Cosserat-type rods. In: Altenbach, H and Eremeyev, VA (eds.) *Generalized continua from the theory to engineering applications (CISM International Centre for Mechanical Sciences, vol. 541)*. Vienna: Springer, 2013, 179–248.
- [76] Luongo, A, and Zulli, D. *Mathematical models of beams and cables*. Hoboken, NJ: Wiley, 2013.
- [77] Eremeyev, VA, and Altenbach, H. Basics of mechanics of micropolar shells. In: Altenbach, H and Eremeyev, VA (eds.) *Shell-like structures (CISM International Centre for Mechanical Sciences (Courses and Lectures), vol. 572)*. Cham: Springer, 2017, 63–111.
- [78] Turco, E, Misra, A, Pawlikowski, M, et al. Enhanced Piola–Hencky discrete models for pantographic sheets with pivots without deformation energy: Numerics and experiments. *Int J Solids Struct* 2018; 147: 94–109.
- [79] dell'Isola, F, Cuomo, M, Greco, L, et al. Bias extension test for pantographic sheets: Numerical simulations based on second gradient shear energies. *J Eng Math* 2017; 103(1): 127–157.
- [80] Greco, L, Giorgio, I, and Battista, A. In plane shear and bending for first gradient inextensible pantographic sheets: Numerical study of deformed shapes and global constraint reactions. *Math Mech Solids* 2017; 22(10): 1950–1975.